PIER M

Numerical Modeling of GPR for Underground Multi-Pipes Detection by Combining GprMax and Deep Learning Model

Qiang Guo[1], Pengju Yang[1, 2, *], Rui Wu[1, 3], and Yuqiang Zhang[1]

[1]*School of Physics and Electronic Information, Yan'an University, Yan'an 716000, China*
[2]*Key Laboratory for Information Science of Electromagnetic Waves (MoE), Fudan University, Shanghai 200433, China*
[3]*Institute for Radio Frequency Technology and Software, Beijing Institute of Technology, Beijing 100081, China*

ABSTRACT: As a popular nondestructive technique, ground penetrating radar (GPR) is extensively utilized for detecting underground pipelines. In this paper, an efficient and automatic scheme is presented for the detection and classification of underground pipelines by combining electromagnetic modeling and machine learning techniques. By virtue of open-source gprMax software, the B-scan signatures of underground pipelines are simulated and analyzed in detail, with four types of underground pipelines taken into account, i.e., iron pipelines, concrete pipelines, copper pipelines, and PVC pipelines. On the basis of electromagnetic modeling, B-scan profiles of underground pipelines are preprocessed by using the average method and time gain compensation method to obtain a dataset for training neural network of YOLOv8 model. The simulations indicate that our scheme combining simulated B-scan profiles and YOLOv8 model is able to detect and classify underground pipelines with high accuracy, and the category and material of underground pipelines can be determined with a high confidence level. Specifically, the detection time of a single B-scan image for underground pipelines is about 0.02 s, and the average detection accuracy can reach 0.995, which is potentially valuable for the automatic detection and classification of underground pipelines in GPR applications.

1. INTRODUCTION

With the process of accelerated urbanization, underground pipelines, which function as the "arteries" of urban operation, play a crucial role in the construction of urban infrastructure. However, urbanization is often characterized by insufficient construction precision, improper planning, and other issues, frequently damaging underground pipelines. Current pipeline detection methods can be divided into destructive testing (DT) and nondestructive testing (NDT). Although DT can provide accurate information about underground pipelines, it is time consuming, labor intensive, and can cause damage to underground pipelines or other infrastructures. In contrast, NDT methods, such as acoustic method and resistivity tomography, offer less intrusive alternatives. Among these, ground-penetrating radar (GPR) has emerged as a highly effective tool for detecting underground pipelines, largely due to its straightforward operation, high resolution, and extensive detection range [1].

Usually, underground pipelines are metal or non-metallic pipelines. The distinct physical properties of pipelines and the surrounding soil make GPR an ideal detection tool [2]. The hyperbolic shape of pipeline radar profiles is the most significant feature for detecting pipeline targets. Consequently, the symmetry of the hyperbolic shape can be used to quickly identify hyperbolic features in B-scan profiles [3]. However, in reality, the collected GPR images are not direct representations of the underground targets. Therefore, data interpretation requires

substantial professional knowledge, largely depending on the experience level of the data processing personnel. Moreover, the manual identification and classification of the pipeline radar images is time consuming and prone to error, due to the interlacing of underground pipelines in urban areas and the variable composition of soil. These factors can lead to miscalculations and omissions in judgment, escalating the risk of urban infrastructure and maintenance issues, and potentially endangering public safety. Therefore, it is paramount to improve the precision and efficacy of pipeline profiles interpretation to ensure the secure operation of underground pipelines and minimize urban operations risks.

With the continuous advancement of artificial intelligence (AI) technology, AI-based methods have attracted significant attention from scholars for pipelines detection and classification by using the hyperbolic characteristics of underground pipelines [4–6]. For example, Kaur et al. used a new robot equipped with ground-penetrating radar sensors to perform measurements and achieved effective classification and detection of bridge reinforcement bars by combining support vector machines with directional gradient histogram features [7]. A column-connected clustering algorithm and orthogonal distance hyperbolic fitting algorithm were proposed in [8], enabling efficient separation of the multi-target regions in ground-penetrating radar data. Pasolli et al. analyzed the ground-penetrating radar data by using a combination of pattern recognition and support vector machines [9]. Wong et al. proposed a multivariate and classified corrosion state of concrete by using a logistic regression method [10]. Xue et al. combined GPR

---

* Corresponding author: Pengju Yang (pjyang@fudan.edu.cn).

and a machine learning model to classify and identify rock layers [11]. Xue et al. proposed an efficient method that combines robust principal component analysis (RPCA) and backpropagation (BP) neural networks to detect and locate underground targets in urban roads using GPR images [12]. Ref. [13] presents a novel method for early breast cancer detection and classification using non-ionizing microwave signals and the YOLOv5 deep learning algorithm to analyze backscatter data and create accurate tumor images. These studies demonstrate the feasibility and efficacy by combining AI and GPR for the detection and classification of underground pipelines. However, the performance of neural networks is usually affected by uncertainties and/or inaccuracies of the available datasets for training neural networks including measured and simulated GPR data. Fuzzy logic may be an effective way to improve the ability to correctly classify the analyzed data, offering greater robustness and reliability in the interpretation of the results [14].

Aiming at the problem of underground pipelines detection and classification, this paper is devoted to developing an efficient and automatic scheme by combining electromagnetic modeling and machine learning techniques. By virtue of open-source gprMax software, the B-scan signatures of underground pipelines are simulated and analyzed in detail, in which real soil is approximately simulated by using a semi-empirical soil model. To obtain a proper dataset with more distinct hyperbolic features for training neural network, B-scan profiles of underground pipelines are preprocessed by using the average method and time gain compensation method. To enhance the diversity of the training data, improve the model's generalization ability, and reinforce the model's robustness, the preprocessed B-scan profiles are processed using data enhancement techniques. On the basis of the generated B-scan dataset, the deep learning model of you only look once version 8 (YOLOv8) is utilized for the detection and classification of underground pipelines, owing to its higher accuracy and faster detection speed than the previous versions of YOLO.

This paper is organized as follows. Section 2 introduces the principle of GPR and electromagnetic (EM) modeling of underground pipelines. In Section 3, the dataset generation and the performance indexes of YOLOv8 are presented. In Section 4, results and analyses are presented, including the performance indexes of the YOLOv8 model for detecting and classifying different types of underground pipelines, which is also used to detect and classify multi-pipelines. Section 5 concludes this paper.

2. EM MODELING OF UNDERGROUND PIPELINES USING GPRMAX

GPR is a nondestructive geophysical technique for detecting the distribution of substances within a medium. This method operates on the principles of reflection, refraction, and bypassing of high-frequency pulsed electromagnetic waves underground, aiming to accurately identify underground structures and properties. GPR offers a high-resolution accuracy down to the order of centimeters, allowing it to the order of determining the buried depths, sizes, shapes, and orientations of objects [15]. In recent years, GPR has emerged as an important technol-

ogy in geophysical exploration due to its straightforward operation, high resolution, and nondestructiveness, etc. [9, 16]. It has been employed in several fields, including underground imaging [17, 18], road detection [19–21], landmine detection [22], and the resolution of numerous technical challenges, which has great potential and broad application prospects.

2.1. 2D Maxwell's System for GPR Applications

Considering two-dimensional Maxwell's equations, we assume that all physical quantities are independent of the y-coordinate. This assumption leads to the formation of two decoupled systems, namely transverse electric (TE) mode and transverse magnetic (TM) mode. The decoupling equations for the TE and TM modes in the two-dimensional time domain are as follows.

$$\frac{\partial E_y}{\partial z} = -\mu \frac{\partial H_x}{\partial t} \tag{1}$$

$$\frac{\partial E_y}{\partial x} = \mu \frac{\partial H_z}{\partial t} \tag{2}$$

$$\varepsilon \frac{\partial E_y}{\partial t} + \sigma E_y = \frac{\partial H_z}{\partial x} - \frac{\partial H_x}{\partial z} + J_y \tag{3}$$

$$\frac{\partial H_y}{\partial z} = \varepsilon \frac{\partial E_x}{\partial t} + \sigma E_x + J_x \tag{4}$$

$$-\frac{\partial H_y}{\partial x} = \varepsilon \frac{\partial E_z}{\partial t} + \sigma E_z + J_z \tag{5}$$

$$\mu \frac{\partial H_y}{\partial t} = \frac{\partial E_x}{\partial z} - \frac{\partial E_z}{\partial x} \tag{6}$$

where σ, ε, and μ are the electrical conductivity, dielectric constant, and magnetic permeability of the medium, respectively. These scalar field quantities are responsive to the electrical properties of a medium. Eq. (1)–Eq. (3) represent the decoupled equations in the TM mode in the 2D-time domain, and Eq. (4)–Eq. (6) are the decoupled equations in the TE mode in the 2D-time domain. Eq. (1)–Eq. (6) are the GPR time-domain control equations with attenuation terms in the two-dimensional case. Inter-well radar is typically modeled using electromagnetic equations in TE mode for forward modeling, while the antenna radiation direction of ground-based GPR is perpendicular to the measurement plane xOz, and it is typically modeled using equations in the TM mode.

The TM mode is frequently employed in GPR applications primarily because, when propagating in the underground medium, the electric field component is perpendicular to the medium interface, while the magnetic field component is parallel to it. The characteristics of the TM mode provide advantages such as robust anti-jamming capability, greater depth of detection, and higher resolution in underground detection.

2.2. GPR B-Scan Echo Acquisition and Its Hyperbolic Signature

The GPR system comprises five components: the central control unit (host), transmitting antenna, receiving antenna, transmitter, and receiver. The transmitting antenna sends radar waves into the ground, while the receiving antenna captures

radar waves reflected from underground targets. The host, which is the core of the system, sends transmission commands to the transmitter and retrieval commands to the receiver, including start and stop times, transmission frequency, repeat counts, and other parameters. The transmitter emits high-frequency pulsed electromagnetic waves into the ground as directed by the host, while the receiver collects data according to the control commands. After sampling and A/D conversion, the received reflection signals are converted into digital signals for display and storage [23]. GPR equipment typically consists of one or more transmitting antennas and one or more receiving antennas, which can be placed on the ground or in boreholes. Most ground-penetrating radar systems use pulsed signals, with the reflected signals recorded in the time domain by a sampling receiver.

GPR data acquisition modes can be categorized into continuous and discrete (point) acquisition modes. Continuous acquisition modes can be further divided into time-triggered and distance-triggered (wheel-triggered) modes. The time-triggered acquisition mode establishes a fixed time interval, ensuring that the time interval between each data channel is consistent. In contrast, the distance-triggered mode sets a displacement interval for acquisition, ensuring equal displacement intervals between every two data channels. In the distance-triggered mode, the GPR initiates data acquisition when the range wheel connected to the antenna reaches a specific distance. Typically, GPR uses the distance-triggered mode to capture accurate target position information.

Figure 1 illustrates the operational principles of GPR and the schematic diagram of a B-scan echo. To detect the underground pipeline, the GPR is moved along the surface of the medium in the direction of the vertical pipeline. Fig. 1(a) is an A-scan schematic, and Fig. 1(b) is a B-scan schematic. B-scan signals are formed by A-scan signals in sequence. As shown in Fig. 1(c), x is the horizontal position of the pipeline target, and x_i is the position of the transmitting antenna. The transceiver antenna begins moving from a position farther from the target and passes over the target and detects according to the displacement interval set by the distance trigger as it moves away from the target. An A-scan data is obtained for each scanning channel, recording the radar's reflected echo signal. The B-scan profile of the GPR is obtained by arranging each channel of A-scan data in sequence. As illustrated in Fig. 1(d), the horizontal coordinate represents the scanning channel information, while the vertical coordinate corresponds to the time axis. From the B-scan profile, the corresponding feature of the GPR for the pipeline target can be observed as a downward-opening hyperbola.

The electromagnetic wave emitted by the transmitting antenna encounters the pipeline target, and the receiving antenna captures the reflected echo from the underground pipeline target. The time recorded by the GPR is the propagation time of the electromagnetic wave traveling to and from the antenna and the pipeline target, referred to as the bi-directional travel time.

$$t_i(x, z) \;=\; \frac{1}{\nu} \cdot \sqrt{\left(z + \frac{R}{2}\right)^2 + (x - x_i)^2}$$
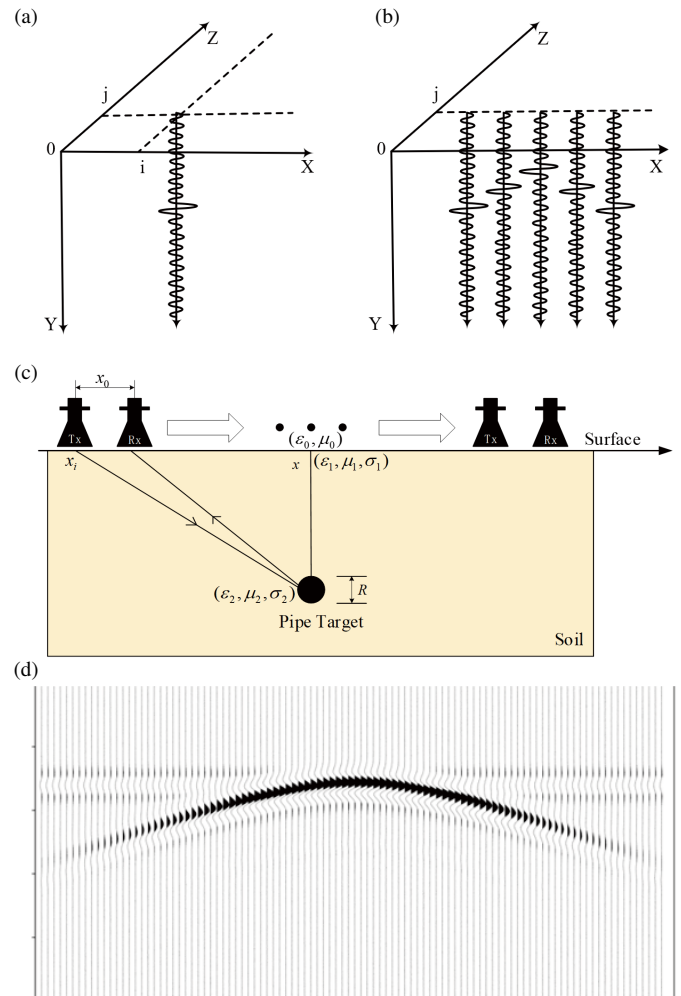

FIGURE 1. Schematic diagram of ground-penetrating radar operation and B-scan echo. (a) A-scan schematic. (b) B-scan schematic. (c) Electromagnetic wave propagation schematic. (d) B-scan echo profile.

$$+\sqrt{\left(z + \frac{R}{2}\right)^2 + (x - x_i - x_0)^2} - R \quad (7)$$

where t_i represents the two-way propagation time of electromagnetic waves; x_0 denotes the distance between the transmitting antenna and the receiving antenna; R represents the pipeline target diameter; Z denotes the pipeline target depth (distance from the surface to the upper surface of the pipeline); and ν represents the electromagnetic wave propagation speed in the medium. The electromagnetic wave propagation speed in the medium is calculated as follows.

$$v = \frac{c}{\sqrt{\varepsilon_r}} \quad (8)$$

where C is the propagation speed of electromagnetic waves in a vacuum (i.e., the speed of light, $C = 3.8 \times 10^8$ m/s), and ε_r represents the relative permittivity of the medium.

Normally, there is a difference between the dielectric constant of the underground pipeline and that of the surrounding soil. When an electromagnetic wave propagates to the pipeline, it produces a distinct reflection, which results in a radar profile
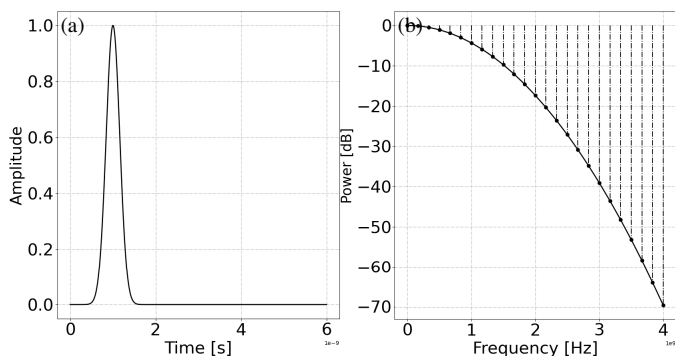
FIGURE 2. Gaussian waveform. (a) Time-domain waveform of the Gaussian waveform. (b) Power spectrum of the Gaussian waveform.

FIGURE 3. Ricker waveform. (a) Time-domain waveform of the Ricker waveform. (b) Power spectrum of the Ricker waveform.

consisting of a single data channel that is characterized by a hyperbolic feature with a downward direction. This opening can be observed in the image.

2.3. gprMax EM Simulator

The gprMax is a professional electromagnetic wave simulation software that employs finite-difference time-domain (FDTD) algorithms [24, 25] and perfectly matched layer (PML) boundary absorption conditions [26]. It is designed to address the propagation and scattering problems of Maxwell's equations in the time domain [27]. The software is used in the simulation of geo-radar and other electromagnetic detection and diagnostic applications. It can simulate electromagnetic waves in a multitude of complex environments, including non-homogeneous and anisotropic media. Furthermore, it supports various source and receiver configurations with different waveforms.

The currently commonly used radar excitation sources include *cont_sine excitation sources*, *sine excitation sources*, *Gaussian excitation sources*, and *Ricker excitation sources*. In gprMax simulations, the Ricker waveform is defined as the negative, normalized second-order derivative of a Gaussian waveform.

$$W(t) = e^{-\zeta(t-\chi)^2} \qquad (9)$$

$$W(t) = -(2\zeta(t-\chi)^2 - 1)e^{-\zeta(t-\chi)^2} \qquad (10)$$

In Eqs. (9)–(10), $\zeta = \pi^2 f^2$, f is the frequency. Eq. (9) represents the Gaussian waveform formula, and Eq. (10) is the Ricker waveform formula.

Figures 2(a) and (b) present the Gaussian pulse waveform in the time domain and its power spectrum, respectively. Figs. 3(a) and (b) show the Ricker waveform in the time domain and its power spectrum, respectively. In Figs. 2 and 3, the center frequency is 1 GHz, with a time window of 6 ns and a time step of 1.926 ps. Generally, the operating frequency range of the GPR is between 10 MHz and 2.5 GHz, and the propagation in the subsurface medium is mainly dominated by displacement currents [28].

Comparing the time-domain waveforms and power spectra of the two waves, it is found that the Ricker wave is preferred in GPR due to its superior energy distribution at both low and high frequencies, resulting in better reflection of subsurface signals.
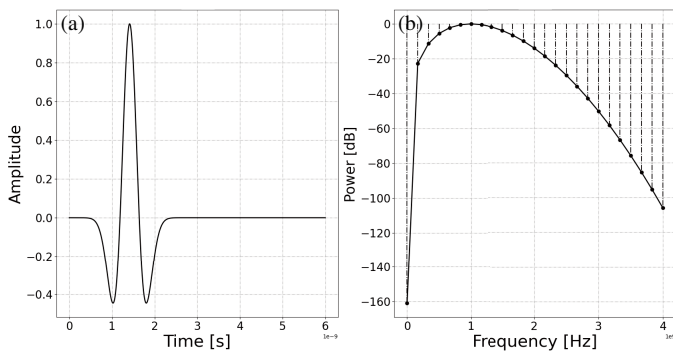
The sharp amplitude peaks provide better time resolution, enabling the radar to detect fine underground targets and provide accurate depth localization information.

2.4. Peplinski's Semi-Empirical Soil Model

When modeling with gprMax, it is necessary to study models that approximate real soil conditions. In this paper, we use a semi-empirical soil model proposed by Peplinski et al. in 1995, as mathematical formulas for the parametric expression of the electromagnetic characteristics of real soils [29]. This theoretical model suggests that the electromagnetic characteristics of soil are determined by two main factors. One factor is the proportion of different particulate components in the soil, and the other is the soil water content. Soil particles can be broadly classified into three categories, clay, silt soil, and sandy soil. Clay particles have a diameter of less than 0.002 mm, while silt soil particles have a diameter between 0.002 mm and 0.05 mm. Sandy particles have a diameter between 0.05 mm and 2 mm. Different ratios of these three soil particles form various soil types, resulting in changes in the soil's dielectric constant and thus different electromagnetic properties. The water content in the soil also plays a crucial role in influencing its electromagnetic properties. Based on the aforementioned theory, Peplinski et al. present a formula for the relative dielectric constant of the soil.

$$\varepsilon = \varepsilon' + i\varepsilon'' \qquad (11)$$

$$\varepsilon' = 1.15 \left[1 + \frac{\rho_b}{\rho_s} \left(\varepsilon_s^\alpha \right) + m_\nu^{\beta'} \varepsilon_{f_w}'^\alpha - m_\nu \right]^{1/\alpha} - 0.68 \qquad (12)$$

$$\varepsilon'' = \left[m_\nu^{\beta''} \varepsilon_{f_w}''^\alpha \right]^{1/\alpha} \qquad (13)$$

The complex soil dielectric constant ε proposed by Peplinski et al. consists of a real part ε' and an imaginary part ε''. In Eqs. (11) and (12), ρ_b and ρ_s denote the density of the soil and the density of sand particles in the soil, respectively. m_ν represents the volumetric water content of the soil, and α is an empirically relevant constant, which is taken here as 0.65 for typical soil.

$$\beta' = 1.2748 - 0.519S - 0.152C \qquad (14)$$

$$\beta'' = 1.33797 - 0.603S - 0.166C \tag{15}$$

where β' and β'' are expressed as shown in Eqs. (14) and (15), determining the proportions of the three constituents of the soil. Here, S represents the proportion of sandy soil, and C represents the proportion of clay in the soil.

$$\varepsilon'_{fw} = \varepsilon_{w\infty} + \frac{\varepsilon_{w0} - \varepsilon_{w\infty}}{1 + (2\pi f \tau_w)^2} \tag{16}$$

$$\varepsilon''_{fw} = \frac{2\pi f \tau_w (\varepsilon_{w0} - \varepsilon_{w\infty})}{1 + (2\pi f \tau_w)^2} + \frac{\sigma_{eff}}{2\pi\varepsilon_0 f} \frac{(\rho_s - \rho_b)}{\rho_s m_v} \tag{17}$$

ε'_{fw} and ε''_{fw} appearing in Eqs. (16) and (17) represent the real and imaginary parts of free water in the soil, respectively. $\varepsilon_{w\infty}$ is the limit at which ε''_{fw} higher frequencies are reached; ε_{w0} is the static relative permittivity of water; τ_w is the constant of thermal dynamic equilibrium; σ_{eff} is the effective conductivity.

The preceding analysis defines the electromagnetic properties of Peplinski's semi-empirical soil model. In this study, Peplinski's semi-empirical soil is used as the soil background in the simulation to approximate real soil conditions as closely as possible.

Table 1 presents the parameters of the soil modeled in this study. Through calculations, the dielectric constant of the soil model used in this study is between 2.5 and 3.5, which is consistent with common dry soil with a dielectric constant between 2 and 6 at microwave frequency 500 MHz.

TABLE 1. Compositional parameters of the soil in the model.

component	quantity
Gravel content	0.5
Clay content	0.5
Packing density	2 g/cm^3
Gravel density	2.66 g/cm^3
Volumetric water content	0.001–0.01

Figures 4(a)–(b) show the real soil profile and Pelinski's semi-empirical soil profile, respectively. In Fig. 4(a), we observe that the soil is composed of particles of various sizes. This heterogeneous distribution results in a dielectric constant that is nonuniform and randomly varying. In Fig. 4(b), the soil is electromagnetically modeled using the values from Table 1, aiming to replicate the real soil as closely as possible for the underground soil.
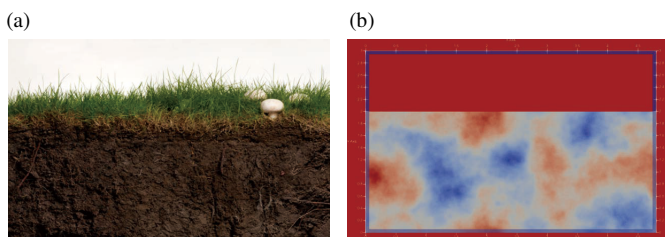
(a)   (b)

FIGURE 4. Soil profiles. (a) Real soil profile. (b) Pelinski's semi-empirical soil profile.

2.5. EM Modeling of B-Scan Profile for Underground Pipelines

The electromagnetic modeling of underground pipelines employs gprMax to simulate B-scan underground pipelines and obtain B-scan profiles of pipeline targets. These profiles are then expanded using Python scripts to create an underground pipeline dataset. The process is illustrated in Fig. 5.

A key aspect of this study is the use of gprMax for the modeling and B-scan imaging of underground pipelines [30]. The dataset uses gprMax software to simulate metallic and non-metallic pipelines in subsurface soil through forward modeling based on the FDTD method [31]. Table 2 shows the electrical parameters of the medium.

TABLE 2. Electrical parameters of the pipeline in the model.

material	relative permittivity	conductivity	permeability
Concrete	6	0.1	1
Iron	1	1e7	150
PVC	3	1e-14	1
Copper	1	5.8e7	1

The spatial extent of the simulation is $4.8\,\text{m} \times 3\,\text{m}$, with a grid size of $0.006\,\text{m} \times 0.006\,\text{m} \times 0.002\,\text{m}$, a time window of 50 ns, and an antenna spacing of 0.04 m. A Ricker wave with an amplitude of 1 and a center frequency of 500 MHz is used as the excitation source for the model simulation. This excitation source is used to perform and generate a B-scan of the pipelines.

Figures 6(a)–(d) show the visualization of the model file using Paraview software [32]. The blue dots represent the simulated pipeline models, and the outermost purple layer indicates the absorbing boundary condition. PML absorbing boundary condition is used to simulate electromagnetic wave propagation in an infinite space. This boundary condition minimizes the effect of the boundary reflections on the simulation results.

Figures 7(a)–(d) show the echoes obtained from B-scanning of the pipe models in Figs. 6(a)–(d) using gprMax. The original B-scan plots include direct and pipe echoes. Figs. 8(a)–(d) show the B-scan hyperbolic echoes after processing the pipe models in Figs. 7(a)–(d) using the average method. Comparing Figs. 8(a)–(d), it can be seen that the echo signal from the metal pipeline is stronger, and the echo signal of the non-metal pipeline is weaker. This difference is due primarily to differences in electromagnetic characteristics. Metal pipelines have strong electromagnetic reflection signals, making their echo signals more prominent in B-scan images. In contrast, non-metal pipelines have weaker electromagnetic reflections, leading to less distinct echo signals, which increases the difficulty of detection.

2.6. Preprocessing of B-Scan Profiles

In GPR, the receiving antenna initially captures the direct wave signal, whereas the return signal from the underground pipeline is attenuated due to electromagnetic wave propagation in the soil. Consequently, the direct wave signal is more prominent in the B-scan diagram, while the return signal from the underground pipelines is less pronounced. To obtain high-quality hy-
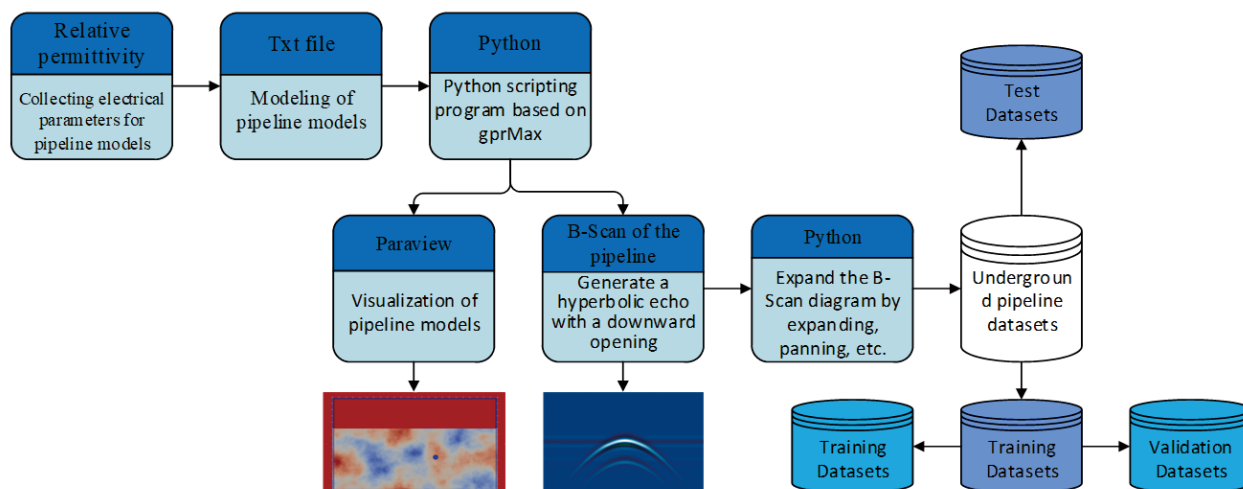
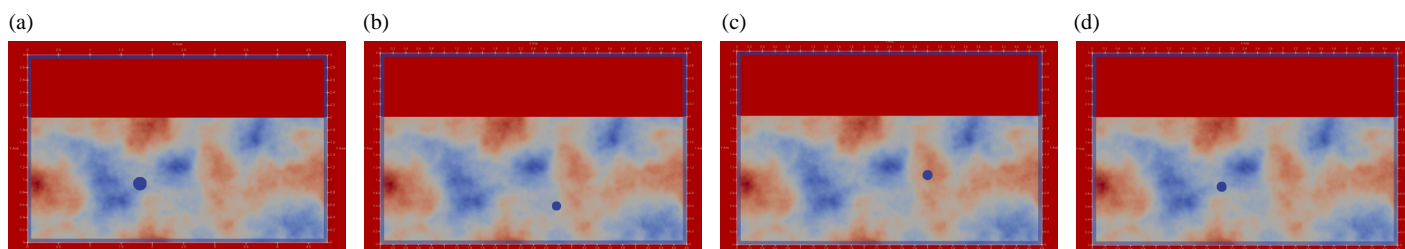**FIGURE 5**. Flowchart for creating an underground pipeline dataset.

FIGURE 6. Visualization of the pipeline models. (a) Concrete pipeline model. (b) Copper pipeline model. (c) PVC pipeline model. (d) Iron pipeline model.
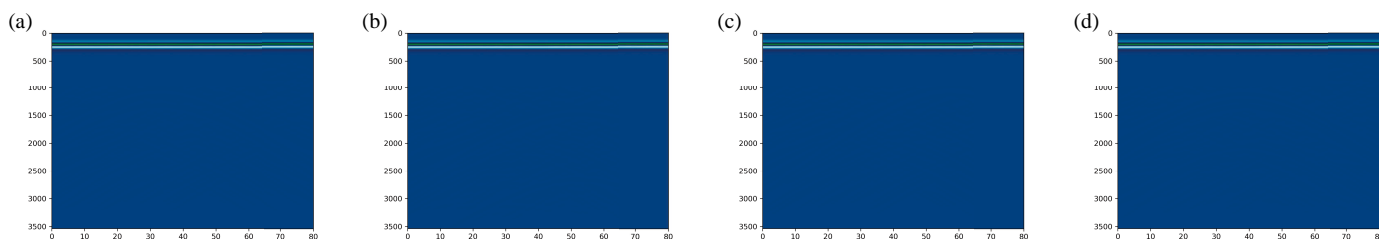

FIGURE 7. Original B-scan profiles of underground pipelines. (a) Concrete pipeline. (b) Copper pipeline. (c) PVC pipeline. (d) Iron pipeline.
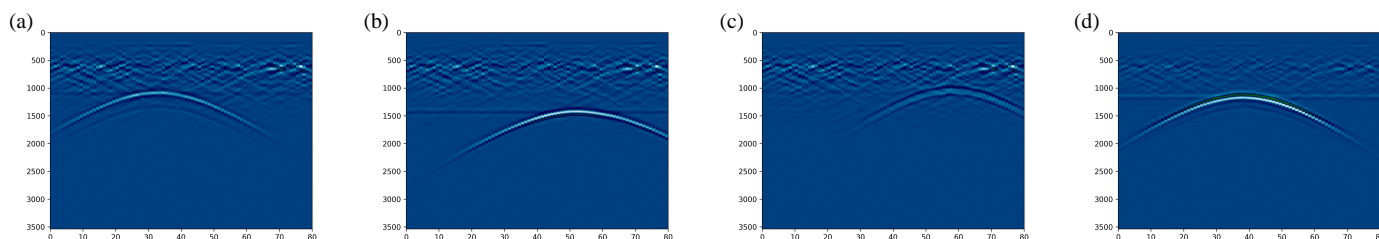

FIGURE 8. B-scan profiles of the pre-processed undergrand pipelines. (a) Concrete pipeline. (b) Copper pipeline. (c) PVC pipeline. (d) Iron pipeline.

perbolic echoes, this study applied the average method to process the difference between the target echo signal and the direct wave, and the target echoes were enhanced using the time gain compensation function.

The average method involves dividing the image data into several $n * n$ matrices and then averaging the pixels within each matrix template to replace the original pixel values. Upon detecting the target body with GPR, the acquired B-scan im-

age comprises multiple A-scan measurements along a survey line, assuming that there are N channels. Each set of A-scans contains numerous sample points, considering that there are M sample points. Therefore, the B-scan data forms an $M \times N$ matrix denoted as D_{ij}. The average method involves averaging each row of data within the matrix. Thereafter, the average value of each row is subtracted from each row of data within the matrix, thereby achieving a direct wave deal.

$$S_{ij} = D_{ij} - \frac{1}{N} \sum_{j=1}^{N} D_{ij} \qquad (18)$$

The amplitude of electromagnetic waves tends to decay rapidly during their propagation through the ground due to the presence of substances such as gravel in the simulated soil. This results in that the target echo, after the removal of the direct wave, cannot reach the required level. Therefore, the time gain compensation function is used to amplify the target echo. The time gain compensation is achieved through the time-varying amplitude compensation method for the depth echo signal. It is observed that the energy of general electromagnetic waves changes by the law of exponential decay. Using exponential gain can significantly reduce the interference caused by human correction.

$$y = a^x - 0.5 \qquad (19)$$

In Eq. (19), x represents the sampling rate. In this study, the base a is set to 3, and the maximum gain is limited to 800. The exponential form of time gain is a nonlinear form of gain and grows very fast. Therefore, the maximum gain must be limited when time gain compensation is used to avoid infinite growth.

In Fig. 9, the targets of the four pipelines were placed in uniform and Pelinski's semi-empirical soil, respectively. The B-scans of the pipelines were forward simulated using gprMax. Fig. 9(a) shows the B-scan profile under a uniform medium, while Fig. 9(b) shows the B-scan profile under Pelinski's semi-empirical soil. From Fig. 9(a), it can be observed that the soil background of the homogeneous medium is smoother. This does not correspond to the random distribution of the medium within the soil in real life. From Fig. 9(b), it can be observed that the background of the semi-empirical soil is relatively complex, which more closely resembles the complexity and diversity of real soil and can more accurately reflect the electromagnetic properties of the soil [33].
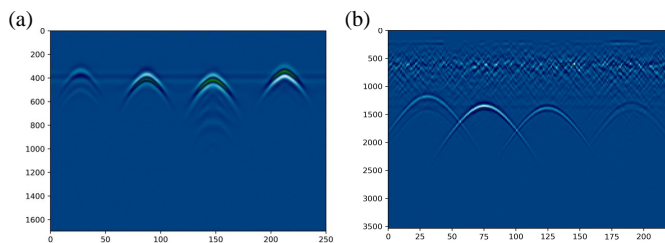

FIGURE 9. B-scan profiles of multi-pipelines. (a) Multiple pipelines under uniform soil. (b) Multiple pipelines under Pelinski's semi-empirical soil.

3. DETECTION OF UNDERGROUND PIPELINES USING YOLOV8 NETWORK

This study employs supervised learning with the YOLOv8 network to achieve intelligent detection and classification of underground pipelines. The implementation process is illustrated in Fig. 10. Fig. 10 depicts the flowchart of supervised learning of the pipeline dataset in the network. This comprises four principal sections: data collection and construction, data analysis and preprocessing, model learning and optimization, and model evaluation and application [34]. As shown in Fig. 10, the primary objective of data collection and construction is the characterization of the pipeline model. In this study, this primarily entails the collection of data on underground pipelines and the modeling of pipelines to create a dataset. In the data analysis and preprocessing section, the primary mandate is to manually label the B-scan profiles. In the data analysis and preprocessing phase, the primary mandate is to manually label the B-Scan profiles. In the stage of Model Learning and Optimization, the YOLOv8 model is employed to monitor feature learning in the B-Scan profiles of pipeline targets. In the stage of Model Evaluation and Application, the pipeline targets are identified and classified using the optimal model from the stage of Model Learning and Optimization.

3.1. Dataset Generation and Enhancement of B-Scan Profile for Neural Network

Another crucial aspect of this study is the dataset creation. The data enhancement technique employed in this study encompasses both offline and online enhancement techniques. The offline enhancement technique involves implementing geometric transformations on the original images. The online technique involves applying geometric and color transformations to the images using data enhancement techniques.

3.1.1. Dataset Generation of B-Scan Profile for Neural Network

The pipelines were first modeled using Python scripts, comprising four materials at different depths, diameters, and locations. Subsequently, all models were subjected to getting B-scans using gprMax, resulting in 2000 B-scan profiles of the four materials' pipelines. After that, the dataset was expanded using enhanced technology, resulting in the generation of 8,000 sheets. A total of 7,200 sheets (1,800 sheets for each of the four materials) were selected as the training dataset, while the remaining 800 sheets were designated as the testing dataset. The training set is divided into 6,480 training sets and 720 validation sets according to a 9 : 1 ratio. The B-scan profiles of the training dataset are manually labeled, with the labels representing the actual frame of the target.

Figure 11(a) shows a schematic diagram of labeling, and Fig. 11(b) shows a schematic diagram of the distribution of the number, location, and size of the labeled pipeline models labeled. From Fig. 11(b), it can be seen from the bar chart in the upper left corner that the number of all four pipelines is greater than 1,600, which is relatively close to each other. As demonstrated by the box plot in the upper right corner, the labels of all B-scan plots are relatively centralized. As illustrated by the
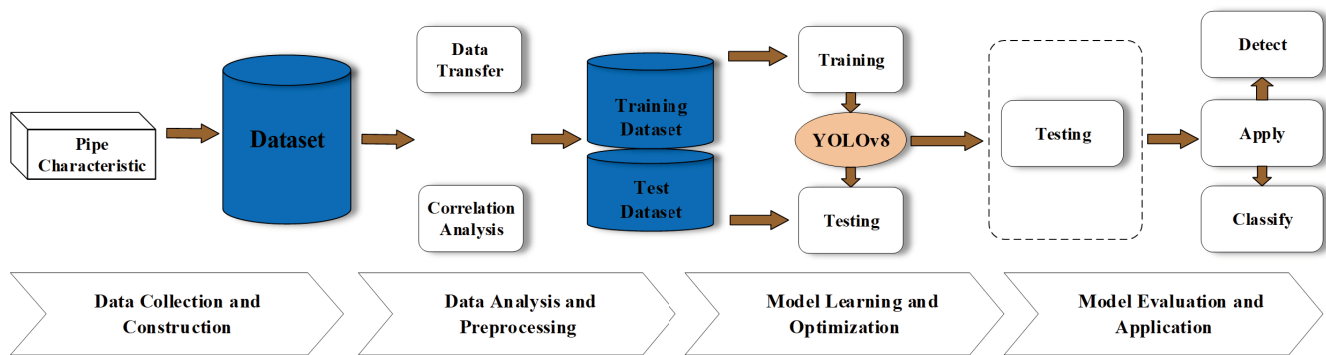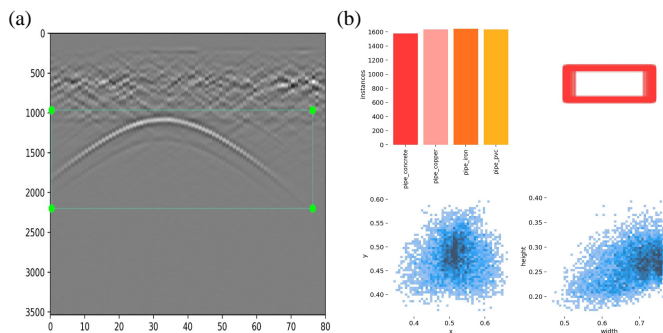
FIGURE 10. Flowchart of supervised learning.

FIGURE 11. Dataset labeling. (a) B-scan labeling. (b) Dataset labeling distribution.

scatter plot in the lower left corner, the center points are primarily dispersed throughout the entire radar profiles. As shown by the heat map in the lower right corner, the widths of the labels are primarily distributed between 0.5 and 0.8. The heights of the labels are predominantly concentrated between 0.2 and 0.35.

3.1.2. Dataset Enhancement of B-Scan Profile for Neural Network

To enhance the diversity of the training data, improve the model's generalization ability, and reinforce the model's robustness, the B-scan plots are subjected to data enhancement techniques. The enhancement techniques encompass geometric, color space, and hybrid transformations. In this study, we primarily employ horizontal flip and translation in geometric transformations and contrast enhancement in color space transformations.

In Fig. 12, (a) shows an original B-scan profile; (b) shows the B-scan profile after panning; (c) shows a B-scan profile after flipping; and (d) shows a B-scan profile after contrast enhancement. Fig. 12 demonstrates the B-scan profiles following data augmentation. The purpose of data enhancement techniques is to expose the model to a wide array of scenarios during training, allowing it to learn generalized feature representations. This process improves the model's adaptability and generalization to various situations. Increasing dataset size through data augmentation techniques helps mitigate the issue of imbalanced samples.

3.2. YOLOv8 Network Structure

YOLOv8 is an efficient target detection algorithm that holds a significant position in the fields of deep learning and computer vision. YOLOv8 inherits the high-speed detection of its predecessor and further optimizes the model's accuracy and generalization abilities. By introducing a more advanced neural network architecture, an improved loss function, and refined feature extraction techniques, YOLOv8 can achieve fast and accurate detection of targets across various scales and categories while maintaining a high frame rate. Additionally, YOLOv8 has particularly enhanced its small target detection capabilities, demonstrating excellent performance in multi-target tracking, real-time video analysis, and other application scenarios. Through continuous research and optimization, YOLOv8 can advance real-time target detection technology and provide robust technical support for intelligent video surveillance, unmanned vehicles, robot vision, and other fields [35, 36].

YOLOv8 improves target detection accuracy by using Darknet-53 as the backbone network (which has powerful feature extraction capabilities), introducing the feature pyramid networks (FPN) structure (which extracts semantic information from feature maps at different scales), and employing bag-of-freebies (BoF) and bag-of-specials (Bos) technologies. BoF increases the diversity of training data through enhancement and optimized strategies, improving robustness and generalization. BoS enhances the network's attention mechanism and feature expression through special operations like sharpness aware minimization (SAM) and convolutional block attention module (CBAM). The network structure is shown in Fig. 13.

3.3. Performance Index of YOLOv8

YOLOv8 uses several performance metrics including classification loss (VFL Loss), regression loss (CIoU Loss), precision, and recall. These metrics measure the generalization ability of the algorithm and its capacity to adapt to new samples.

3.3.1. Confusion Matrix Index

Confusion matrix (as depicted in Table 3) is a widely used tool for assessing the performance of classification models. It provides a visual representation of the discrepancies between actual and predicted values in the model's classification re-
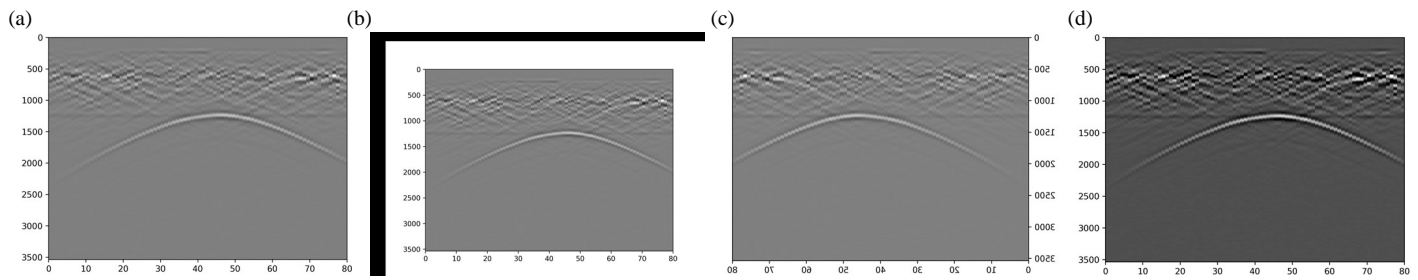
FIGURE 12. B-scan profile of an underground pipe model using data enhancement techniques. (a) Original image. (b) Image after panning. (c) Image after flipping. (d) Image after increasing contrast.
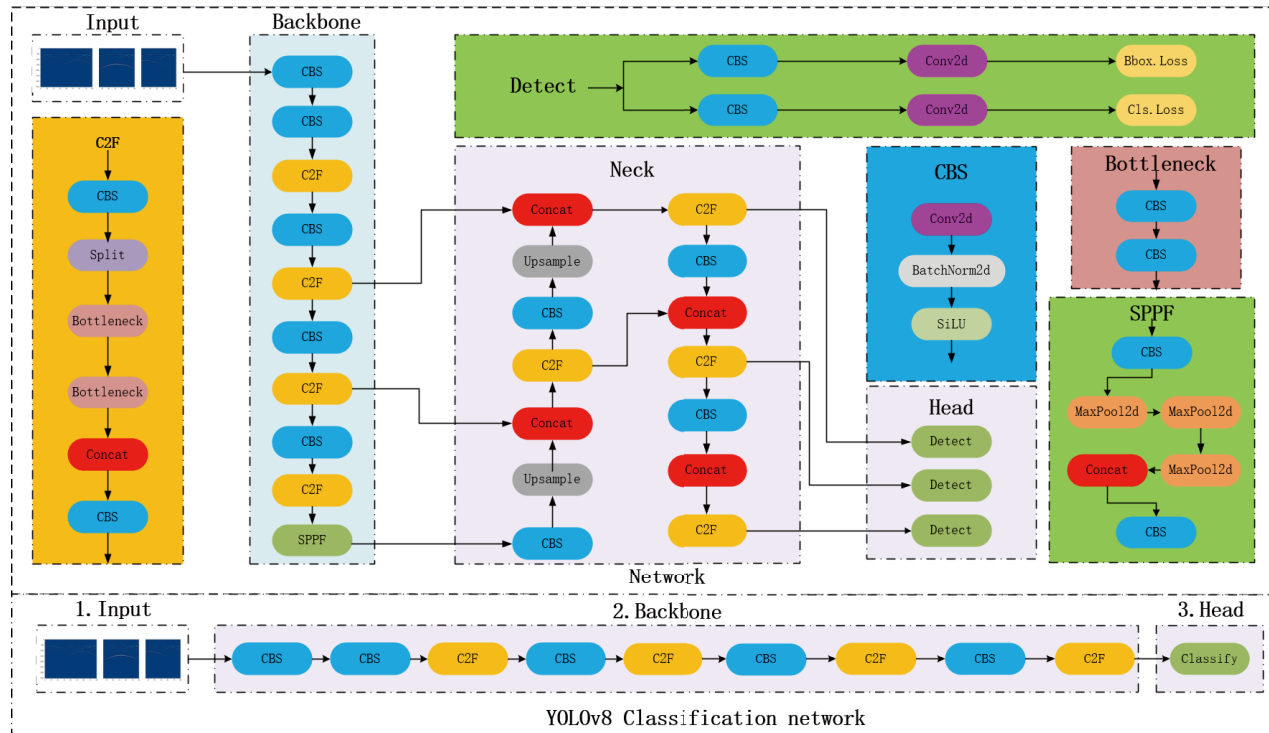

FIGURE 13. YOLOv8 network structure.

sults. Confusion matrix encapsulates the predicted outcomes of a classification problem. It categorizes the true positives, false positives, true negatives, and false negatives for each class, illustrating the specific areas where the classification model makes errors. The matrix reveals if and where the model misclassifies instances across different classes.

In Table 3, TP (True Positive) indicates the number of samples correctly predicted to be stable. FN (False Negative) refers to the number of samples that are actually stable but incorrectly predicted as destabilized. FP (False Positive) represents the number of samples that are actually destabilized but incorrectly predicted as stable. TN (True Negative) indicates the number of samples correctly predicted to be destabilized [37].

3.3.2. Recall Index

Recall, also referred to as the true positive rate, is an essential metric in classification problems. As a significant performance

TABLE 3. Confusion matrix.

		Prediction Outcome		
		p	**n**	
	p′	True positive	False negative	P′
Actual value				
	n′	False positive	True negative	N′
		P	N	

measure in machine learning and statistics, it quantifies the proportion of actual positives correctly identified by the model relative to all actual positive samples. Recall values span from 0
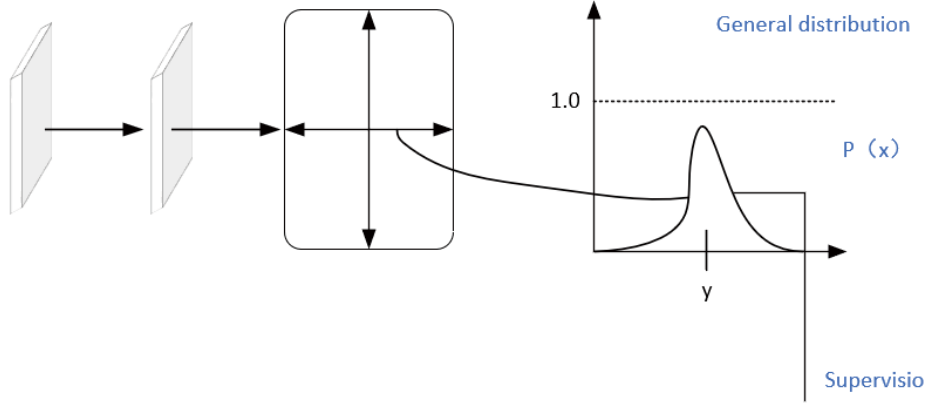
FIGURE 14. Schematic diagram of DFL.

to 1. A higher recall indicates that the model misses fewer positive samples [38]. Enhancing recall usually results in reduced precision (i.e., the ratio of correctly predicted positive samples to all predicted positive samples) because the model may incorrectly classify more samples as positive rather than negative. Therefore, a balance must be struck between increasing recall and maintaining precision in practice. The F1 score evaluates model performance through the harmonic mean of precision and recall [39]. Its value ranges from 0 to 1, with 1 denoting the ideal performance in both precision and recall and 0 indicating extremely poor performance.

$$\text{Precision} = \frac{TP}{TP + FP} \qquad (20)$$

$$\text{Recall} = \frac{TP}{TP + FN} \qquad (21)$$

$$F_1 = \frac{2TP}{2TP + FN + FP} \qquad (22)$$

Eqs. (20) and (21) are precision and recall, respectively. Eq. (22) is the formula for the F1 function.

3.3.3. Loss Function Index

The loss function is essential in machine learning as it quantifies the difference between the predicted and actual values of a model. During model training, the primary goal is to minimize the loss value, as reducing the loss function generally correlates with improved prediction accuracy. Different machine learning tasks and model architectures may require different loss functions.

YOLOv8 introduces Distribution Focal Loss (DFL) in its target detection framework. DFL aims to enhance the performance of the target detection model in handling various scales and imbalanced datasets. It is an optimization over the original Varifocal Loss (VFL), a loss function that combines classification and localization tasks to improve the model's accuracy in predicting target categories and bounding boxes.

$$\text{VFL}(p, q) = \begin{cases} -q(q \log(p) + (1 - q) \log(1 - p)) & q > 0 \\ -\alpha p^{\gamma} \log(1 - p) & q = 0 \end{cases} \qquad (23)$$

where P is the label, and the positive samples q are the IoU of bbox and gt.

The regression loss in YOLOv8 combines complete intersection over union (CIoU) Loss and DFL. CIoU Loss is an enhanced version of the Intersection over Union (IoU) loss function for bounding box regression in target detection. Compared to the traditional IOU loss, CIOU Loss considers the bounding box overlap area, centroid distance, and aspect ratio, enabling the model to predict bounding boxes more accurately.

$$\mathcal{L}_{\text{CIoU}} = 1 - \text{IoU} + \frac{1}{c^2} \rho^2(b, b^{\text{gt}}) + \alpha \nu \qquad (24)$$

In Eq. (24), Intersection over Union (IoU) represents the ratio of the overlap area between the predicted and actual frames to the union area. b and bgt denote the centroids of the predicted and ground truth rectangular frames; ρ denotes the Euclidean distance between the centroids of the two rectangular frames; c denotes the diagonal length of the smallest enclosing box covering the two rectangular frames; ν measures the consistency of the aspect ratios of the two rectangular frames; and α is the weighting coefficient.

The purpose of DFL is to enable the network to quickly focus on values close to the label, maximizing the probability density at the label. The idea is to use the cross-entropy function to optimize the probabilities of the two positions adjacent to the label y. It focuses the network's distribution on the label value.

$$\begin{aligned} \text{DFL}(S_i, S_{i+1}) = & -((y_{i+1} - y) \log(S_i) \\ & + (y - y_i) \log(S_{i+1})) \end{aligned} \qquad (25)$$

where S_i is the sigmoid output of the network; y_i and y_{i+1} represent the order of intervals around the label; and y is the label value.

By combining CIoU Loss and DFL (as shown in Fig. 14), YOLOv8 can more efficiently handle classification and localization tasks in target detection, particularly in multi-scale and complex backgrounds. DFL helps the model better understand and predict various targets by focusing on data distribution characteristics, while CIoU Loss ensures accurate spatial localization. This combination of loss functions provides YOLOv8
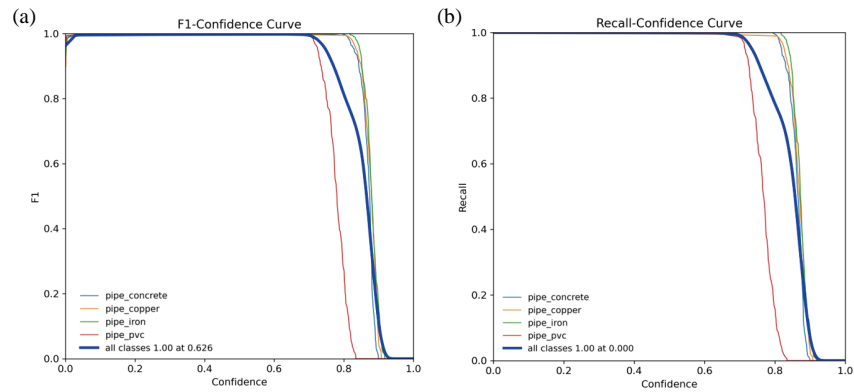
FIGURE 15. Model training results of F1 and recall. (a) F1 index. (b) Recall index.
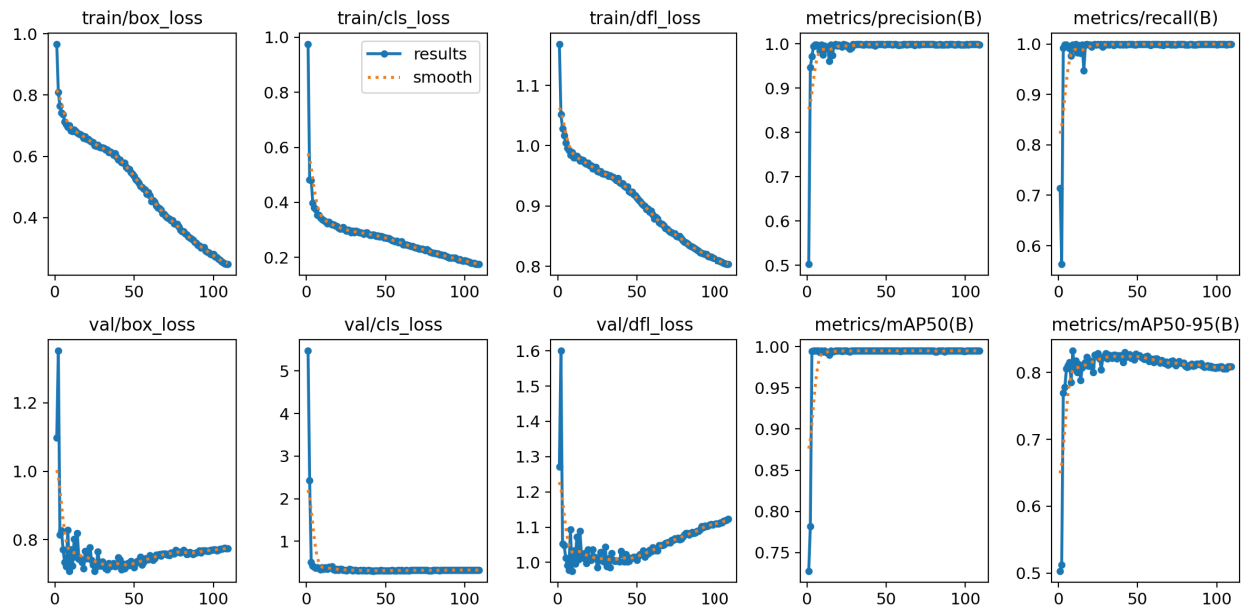

FIGURE 16. Loss function for YOLOv8 training.

with high efficiency and accuracy in addressing complex target detection tasks.

In Fig. 14, y is the distance from the center to an edge divided by the current sampling multiplier. This loss of position around the learned labels can enhance the generalization of the model for occluded and moving objects.

4. RESULTS AND ANALYSIS

4.1. F1 Curve and Recall Curve

Figure 15(a) presents the F1 curve after training the four pipeline models with YOLOv8, while Fig. 15(b) presents the recall curve after training the same models using YOLOv8. As shown in Fig. 15(a), the F1 scores for each type of pipe decrease rapidly from 1 as the confidence threshold increases. At a confidence threshold of around 0.8, the F1 scores for all categories reach 1, indicating accurate predictions for all categories. As shown in Fig. 15(b), the recall for all types of pipes decreases rapidly as the confidence threshold increases.

At a confidence threshold close to 0, the recall is 1, meaning that the model does not miss any positive samples. As the confidence threshold increases, the model begins to miss more samples, and recall decreases. The analysis of Fig. 15(b) shows that when the confidence threshold is low, both recall and F1 scores are very high, indicating that the model can detect all pipelines accurately. As the confidence threshold increases, the model begins to miss some pipelines (recall decreases). However, with a higher threshold, the model's predictions are more likely to be correct (i.e., fewer false positives), as evidenced by the initially smooth part of the F1 score curve. At a confidence level of 0.8, the model achieves the optimal balance of detecting all pipeline classes without errors or false positives. Therefore, 0.8 can be chosen as the preferred operating point.

4.2. Loss Functions

In Fig. 16, the results of loss function include *Box Loss*, *Classification Loss*, *Directional Feature Loss*, *Precision and Recall*,
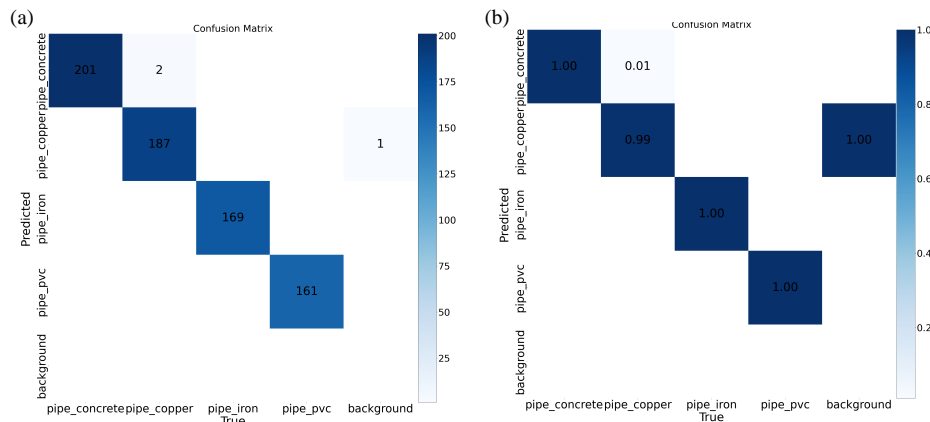
FIGURE 17. Schematic diagram of the confusion matrix. (a) Confusion matrix. (b) Normalized confusion matrix.

and *mAP50*. An analysis of Fig. 16 reveals the following insights,

- **Box Loss:** There is a significant decrease in the loss value over time in both the training and validation phases, indicating improved model performance in locating the bounding box of underground pipelines.
- **Classification Loss:** A decreasing trend is observed in both training and validation phases, suggesting increased accuracy in distinguishing between different types of underground pipelines.
- **Directional Feature Loss:** Decreases in training and validation losses indicate improvements in capturing specific features related to pipeline directional dependence.
- **Precision and Recall:** High values indicate that the model is accurate and not prone to false positives in identifying underground pipelines.
- **mAP50 and mAP50-95:** These metrics show good overall model performance across multiple Intersection over Union (IoU) thresholds.

Combining Fig. 16 with the analysis of the underground pipeline dataset, it is evident that the training and validation performance of the YOLOv8 model on the underground pipeline detection task is steadily improving. Loss values are decreasing, and precision and recall remain high and mean Average Precision (mAP) values increase as training progresses. These metrics indicate that the model excels in learning to accurately detect and classify underground pipelines. In the application of underground pipeline detection, the YOLOv8 model can provide high-confidence detection results, helping to reduce engineering risks and maintenance costs.

4.3. Confusion Matrix

Figure 17(a) shows the predicted results of the YOLOv8 classification model for four pipeline models and backgrounds, compared with the true labels. Fig. 17(b) shows the performance of the YOLOv8 classification model in testing four pipeline models and the background. As observed in Fig. 17(a), the numbers on the diagonal represent the number of correct predictions, i.e., the number of samples where the true category

matches the predicted category. In this confusion matrix, iron pipes are correctly predicted 169 times, copper pipes 187 times, PVC pipes 161 times, and concrete pipes 201 times. The numbers on the non-diagonal lines represent the number of false predictions. As shown in Fig. 17(a), copper pipes were incorrectly predicted as iron pipes 0 times, PVC pipes 0 times, and concrete pipes 2 times. The model performed well in predicting the backgrounds, correctly identifying background samples and misclassifying only one pipe-copper as background. According to the color shade of the confusion matrix (which usually represents the magnitude of the numbers), most predictions are concentrated on the diagonal, indicating high overall model accuracy. As shown in Fig. 17(b), the YOLOv8 model exhibits good classification accuracy for iron, copper, PVC, and concrete pipelines. This indicates that the YOLOv8 model accurately detects these pipeline categories with only two misclassifications. It also shows high accuracy for backgrounds, meaning that backgrounds are correctly classified, and only one background is misidentified as pipelines. There is no indication of cross-misclassification. Normally, cells on the non-diagonal lines would show cases where the model misclassified one class as another. The combination of the confusion matrix and the normalized confusion matrix shows that YOLOv8 performs well in pipeline classification.

4.4. Predicted Results and Discussion

Figures 18(a)–(d) demonstrate the detection, recognition and classification of the test set in the dataset using the trained YOLOv8 model. The confidence score, indicating the certainty level of YOLOv8's recognition results, is also provided [40–42]. In Fig. 18(a), the label "*pipe — concrete 0.88*" indicates that the B-scan profile in this image is a concrete pipe with a 0.88 confidence level. In Fig. 18(b), the label "*pipe — pvc 0.87*" indicates that the B-scan profile in this image is a PVC pipe with 0.87 confidence. In Fig. 18(c), the label "*pipe — copper 0.87*" indicates that the B-scan profile in this image is a copper pipe with 0.87 confidence. In Fig. 18(d), the label "*pipe — iron 0.89*" indicates that the B-scan profile in this image is an iron pipe with a 0.89 confidence level. Comparing the confidence levels of the four pipeline predictions suggests
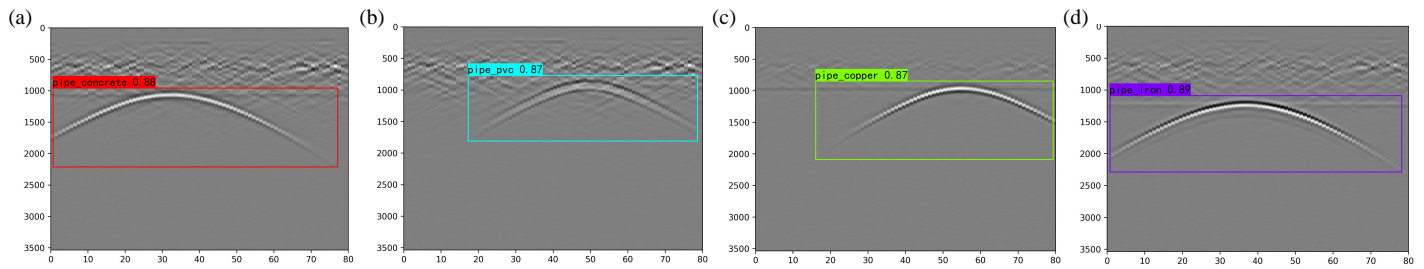
FIGURE 18. Predicted results of underground pipelines using YOLOv8. (a) Concrete pipeline. (b) PVC pipelines. (c) Copper pipelines. (d) Iron pipelines.
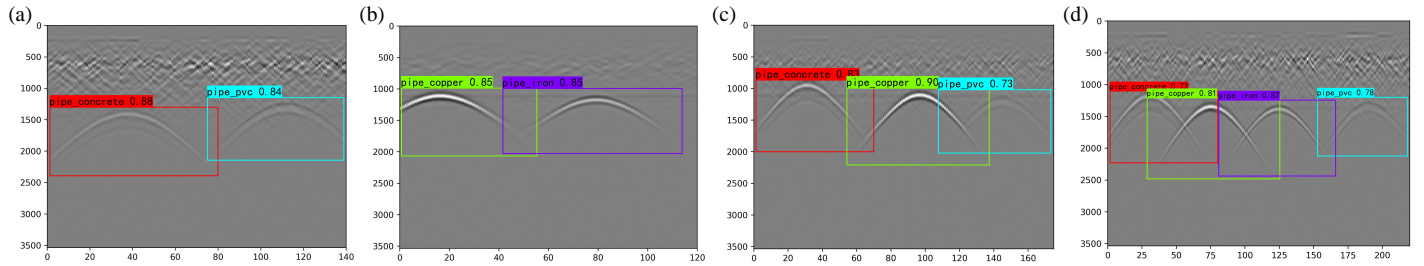

FIGURE 19. Detection and classification of multi-Pipelines. (a) Two pipelines of non-metallic. (b) Two pipelines of metallic. (c) Three pipelines of different materials. (d) Four pipelines of different materials.

that the identification of metallic pipelines consistently exhibits high confidence levels. In contrast, the identification of non-metallic pipelines shows comparatively lower confidence levels. This disparity is attributed to the distinct physical scattering properties of the materials. Metallic pipelines produce clearer and more distinct signals due to their superior conductivity and reflective properties, thereby enhancing the accuracy and reliability of their detection. In contrast, non-metallic pipelines display more varied and less pronounced scattering properties, leading to lower confidence levels in their identification. Analyzing Figs. 18(a)–(d) and their corresponding confidence scores demonstrate the capability of the YOLOv8 neural network model in detecting and classifying different pipeline types. By examining the echo features in the radar images, the YOLOv8 model can accurately determine the material type of the pipelines, offering valuable information for practical applications like urban planning, building construction, and maintenance work.

Figure 19 shows the detection and classification of multi-pipelines. Based on observations from Fig. 19(a) and Fig. 19(b), YOLOv8 demonstrates higher confidence in detecting and classifying both non-metallic and metallic pipelines in double-pipeline scenarios. Observations from Fig. 19(c) show that in triple-pipeline scenarios with metallic pipelines, YOLOv8 exhibits higher confidence for metallic pipelines and lower confidence for non-metallic pipelines. This discrepancy is attributed to the interference caused by reflections from metallic pipelines affecting the detection of non-metallic pipelines. As indicated by Fig. 19(d), YOLOv8 continues to perform well in four-pipe configurations for the detection and classification of underground pipelines. The model's generalization ability is demonstrated through the detection

and classification of multiple pipelines, further validating the feasibility of the method presented in this study.

4.5. Detection Performance Parameters and Discussion

Table 4 presents the resulting parameters for different types of pipes. It includes four performance indexes, Precision, Recall, mAP50, and mAP50-95, as well as the average values of these parameters. Analysis of the parameters indicates that YOLOv8 achieves high accuracy in detecting and classifying underground pipelines. Comparing the results, PVC pipelines show the best overall performance, while concrete pipelines have slightly lower accuracy. Combined with the prediction results in Section 4.4, the detection and classification of pipes using YOLOv8 meet the expected requirements.

TABLE 4. Performance index of validation dataset for different pipes.

class	P	R	mAP50	mAP50-mAP95
all	0.998	0.999	0.995	0.832
pipe-concrete	0.993	1	0.995	0.84
pipe-copper	1	0.995	0.995	0.849
pipe-iron	0.998	1	0.995	0.836
pipe-pvc	1	1	0.995	0.805

However, it is important to underline that the available datasets for training neural networks including measured and simulated GPR data could be affected by uncertainties and/or inaccuracies, negatively influencing the performance of neural networks. These uncertainties can arise from various factors, including the variability of ground conditions, the accuracy of manual labels, and the limited variety of training data. For-

111

tunately, fuzzy logic may be an effective way to improve the ability to correctly classify the analyzed data, offering greater robustness and reliability in the interpretation of the results [14].

5. CONCLUSION

In this paper, the B-scan hyperbolic signatures of underground pipelines are simulated and analyzed by using open-source gprMax. Four types of underground pipelines are taken into account, i.e., iron pipelines, concrete pipelines, copper pipelines, and PVC pipelines. Based on electromagnetic modeling and the average method of B-scan profile for underground pipelines, the dataset of B-scan profile generated by gprMax is utilized for training the YOLOv8 model, and the dataset is labeled using Labelimage for the training set and validation set. To improve the quality and quantity of the dataset, the dataset of the underground pipeline is expanded by using both offline methods (python scripts) and online methods (data enhancement techniques). The trained YOLOv8 model is able to detect and classify underground pipelines with high accuracy, and the category and material of underground pipelines can be determined with a high confidence level. The performance of YOLOv8 for the detection of underground pipelines is validated in terms of confusion matrix, normalized confusion matrix, loss function, F1 function, and recall. The simulations indicate that single or multiple underground pipelines can be efficiently detected and classified by utilizing YOLOv8 with good confidence. The detection time of a single B-scan image for underground pipelines is about 0.02 s, and the average detection accuracy can reach 0.995, which can meet the needs of real-time radar in practical engineering projects. This work is potentially valuable for the detection and classification of underground pipelines in GPR applications. It not only improves the efficiency of underground pipe detection but also reduces the dependence on the operator's skills and time consumption, which brings significant advantages in practical engineering applications. In future work, fuzzy logic will be integrated into our method to enhance uncertainty modeling, improve label accuracy, and enhance the robustness of our deep learning models, particularly in the context of underground pipe detection and classification for both measured and simulated GPR data.

ACKNOWLEDGEMENT

REFERENCES

[1] Frigui, H. and P. Gader, "Detection and discrimination of land mines in ground-penetrating radar based on edge histogram descriptors and a possibilistic K-nearest neighbor classifier," *IEEE Transactions on Fuzzy Systems*, Vol. 17, No. 1, 185–199, 2008.

[2] Muggleton, J. M., M. J. Brennan, and Y. Gao, "Determining the location of buried plastic water pipes from measurements of ground surface vibration," *Journal of Applied Geophysics*, Vol. 75, No. 1, 54–61, 2011.

[3] Sagnard, F. and J.-P. Tarel, "Template-matching based detection of hyperbolas in ground-penetrating radargrams for buried utilities," *Journal of Geophysics and Engineering*, Vol. 13, No. 4, 491–504, 2016.

[4] Tong, Z., J. Gao, and D. Yuan, "Advances of deep learning applications in ground-penetrating radar: A survey," *Construction and Building Materials*, Vol. 258, 120371, 2020.

[5] Bai, X., Y. Yang, S. Wei, G. Chen, H. Li, Y. Li, H. Tian, T. Zhang, and H. Cui, "A comprehensive review of conventional and deep learning approaches for ground-penetrating radar detection of raw data," *Applied Sciences*, Vol. 13, No. 13, 7992, 2023.

[6] Al-Nuaimy, W., Y. Huang, M. Nakhkash, M. T. C. Fang, V. T. Nguyen, and A. Eriksen, "Automatic detection of buried utilities and solid objects with GPR using neural networks and pattern recognition," *Journal of Applied Geophysics*, Vol. 43, No. 2-4, 157–165, 2000.

[7] Kaur, P., K. J. Dana, F. A. Romero, and N. Gucunski, "Automated GPR rebar analysis for robotic bridge deck evaluation," *IEEE Transactions on Cybernetics*, Vol. 46, No. 10, 2265–2276, 2016.

[8] Dou, Q., L. Wei, D. R. Magee, and A. G. Cohn, "Real-time hyperbola recognition and fitting in GPR data," *IEEE Transactions on Geoscience and Remote Sensing*, Vol. 55, No. 1, 51–62, 2017.

[9] Pasolli, E., F. Melgani, and M. Donelli, "Automatic analysis of GPR images: A pattern-recognition approach," *IEEE Transactions on Geoscience and Remote Sensing*, Vol. 47, No. 7, 2206–2217, 2009.

[10] Wong, P. T.-W., W. W.-L. Lai, and C.-S. Poon, "Classification of concrete corrosion states by GPR with machine learning," *Construction and Building Materials*, Vol. 402, 132855, 2023.

[11] Xu, H., J. Yan, G. Feng, Z. Jia, and P. Jing, "Rock layer classification and identification in ground-penetrating radar via machine learning," *Remote Sensing*, Vol. 16, No. 8, 1310, 2024.

[12] Xue, W., K. Chen, T. Li, L. Liu, and J. Zhang, "Efficient underground target detection of urban roads in ground-penetrating radar images based on neural networks," *Remote Sensing*, Vol. 15, No. 5, 1346, 2023.

[13] Kandasamy, L. and S. Reddy, "Deep learning algorithm for automatic breast tumour detection and classification from electromagnetic scattering data," *Progress In Electromagnetics Research C*, Vol. 128, 39–48, 2022.

[14] Versaci, M., G. Angiulli, P. Crucitti, D. D. Carlo, F. Lagana, D. Pellicanò, and A. Palumbo, "A fuzzy similarity-based approach to classify numerically simulated and experimentally detected carbon fiber-reinforced polymer plate defects," *Sensors*, Vol. 22, No. 11, 4232, 2022.

[15] Iftimie, N., A. Savin, R. Steigmann, and G. S. Dobrescu, "Underground pipeline identification into a non-destructive case study based on ground-penetrating radar imaging," *Remote Sensing*, Vol. 13, No. 17, 3494, 2021.

[16] Ganiyu, S. A., M. A. Oladunjoye, O. I. Onakoya, J. O. Olutoki, and B. S. Badmus, "Combined electrical resistivity imaging and ground penetrating radar study for detection of buried utilities in Federal University of Agriculture, Abeokuta, Nigeria," *Environmental Earth Sciences*, Vol. 79, 1–20, 2020.

[17] Iftimie, N., A. Savin, N. A. Danila, and G. S. Dobrescu, "Radar pulses to image the subsurface using Ground Penetrating Radar (GPR)," in *IOP Conference Series: Materials Science and En-*

gineering, Vol. 564, No. 1, 012130, 2019.

[18] Prego, F. J., M. Solla, I. Puente, and P. Arias, "Efficient GPR data acquisition to detect underground pipes," *NDT & E International*, Vol. 91, 22–31, 2017.

[19] Benedetto, A., F. Tosti, L. B. Ciampoli, and F. D'amico, "An overview of ground-penetrating radar signal processing techniques for road inspections," *Signal Processing*, Vol. 132, 201–209, 2017.

[20] Saarenketo, T. and T. Scullion, "Road evaluation with ground penetrating radar," *Journal of Applied Geophysics*, Vol. 43, No. 2-4, 119–138, 2000.

[21] Rasol, M., J. C. Pais, V. Pérez-Gracia, M. Solla, F. M. Fernandes, S. Fontul, D. Ayala-Cabrera, F. Schmidt, and H. Assadollahi, "GPR monitoring for road transport infrastructure: A systematic review and machine learning insights," *Construction and Building Materials*, Vol. 324, 126686, 2022.

[22] Torrione, P. A., K. D. Morton, R. Sakaguchi, and L. M. Collins, "Histograms of oriented gradients for landmine detection in ground-penetrating radar data," *IEEE Transactions on Geoscience and Remote Sensing*, Vol. 52, No. 3, 1539–1550, 2013.

[23] Liu, H., C. Lin, J. Cui, L. Fan, X. Xie, and B. F. Spencer, "Detection and localization of rebar in concrete by deep learning using ground penetrating radar," *Automation in Construction*, Vol. 118, 103279, Oct. 2020.

[24] Ma, X., Y. Li, and J. Song, "A stable auxiliary differential equation perfectly matched layer condition combined with low-dispersive symplectic methods for solving second-order elastic wave equations," *Geophysics*, Vol. 84, No. 4, T193–T206, 2019.

[25] El Mahgoub, K., A. Z. Elsherbeni, and F. Yang, "Dispersive periodic boundary conditions for finite-difference time-domain method," *IEEE Transactions on Antennas and Propagation*, Vol. 60, No. 4, 2118–2122, 2012.

[26] Lu, T., P. Zhang, and W. Cai, "Discontinuous Galerkin methods for dispersive and lossy Maxwell's equations and PML boundary conditions," *Journal of Computational Physics*, Vol. 200, No. 2, 549–580, 2004.

[27] Warren, C., A. Giannopoulos, and I. Giannakis, "gprMax: Open source software to simulate electromagnetic wave propagation for ground penetrating radar," *Computer Physics Communications*, Vol. 209, 163–170, 2016.

[28] Howlader, M. O. F. and T. P. Sattar, "FDTD based numerical framework for ground penetrating radar simulation," *Progress In Electromagnetics Research M*, Vol. 44, 127–138, 2015.

[29] Peplinski, N. R., F. T. Ulaby, and M. C. Dobson, "Corrections to 'Dielectric properties of soils in the 0.3–1.3-GHz range'," *IEEE Transactions on Geoscience and Remote Sensing*, Vol. 33, No. 6, 1340, 1995.

[30] Giannopoulos, A., "Modelling ground penetrating radar by gprMax," *Construction and Building Materials*, Vol. 19, No. 10, 755–762, 2005.

[31] Ayala-Cabrera, D., M. Herrera, J. Izquierdo, and R. Pérez-García, "Location of buried plastic pipes using multi-agent support based on GPR images," *Journal of Applied Geophysics*, Vol. 75, No. 4, 679–686, 2011.

[32] Ahrens, J., B. Geveci, and C. Law, *ParaView: An End-User Tool for Large-Data Visualization*, 717–731, Butterworth-Heinemann, Burlington, 2005.

[33] Soldovieri, F., I. Catapano, P. M. Barone, S. E. Lauro, E. Mattei, E. Pettinelli, G. Valerio, D. Comite, and A. Galli, "GPR estimation of the geometrical features of buried metallic targets in testing conditions," *Progress In Electromagnetics Research B*, Vol. 49, 339–362, 2013.

[34] Gamba, P. and S. Lossani, "Neural detection of pipe signatures in ground penetrating radar images," *IEEE Transactions on Geoscience and Remote Sensing*, Vol. 38, No. 2, 790–797, 2000.

[35] Talaat, F. M. and H. Z. Eldin, "An improved fire detection approach based on YOLO-v8 for smart cities," *Neural Computing and Applications*, Vol. 35, No. 28, 20 939–20 954, 2023.

[36] Yu, H., J. Wang, Y. Han, B. Fan, and C. Zhang, "Research on an intelligent identification method for wind turbine blade damage based on CBAM-BiFPN-YOLOV8," *Processes*, Vol. 12, No. 1, 205, 2024.

[37] Chicco, D., N. Tötsch, and G. Jurman, "The Matthews correlation coefficient (MCC) is more reliable than balanced accuracy, bookmaker informedness, and markedness in two-class confusion matrix evaluation," *BioData Mining*, Vol. 14, No. 1, 1–22, 2021.

[38] Gader, P. D., B. N. Nelson, H. Frigui, G. Vaillette, and J. M. Keller, "Fuzzy logic detection of landmines with ground penetrating radar," *Signal Processing*, Vol. 80, No. 6, 1069–1084, 2000.

[39] Dinh, K., N. Gucunski, and T. H. Duong, "An algorithm for automatic localization and detection of rebars from GPR data of concrete bridge decks," *Automation in Construction*, Vol. 89, 292–298, 2018.

[40] Wang, Y., G. Cui, and J. Xu, "Semi-automatic detection of buried rebar in GPR data using a genetic algorithm," *Automation in Construction*, Vol. 114, 103186, 2020.

[41] Maas, C. and J. Schmalzl, "Using pattern recognition to automatically localize reflection hyperbolas in data from ground penetrating radar," *Computers & Geosciences*, Vol. 58, 116–125, 2013.

[42] Ozkaya, U., F. Melgani, M. B. Bejiga, L. Seyfi, and M. Donelli, "GPR B scan image analysis with deep learning methods," *Measurement*, Vol. 165, 107770, 2020.